energies

MDPI

Article

Multi-Column Semi-Submersible Floating Body Hydrodynamic Performance Analysis

Wei Wang [1,2], Jingyi Hu [1], Cheng Zhao [3,*], Yonghe Xie [1], Xiwu Gong [1,*] and Dingliang Jiang [1]

[1] School of Naval Architecture and Maritime, Zhejiang Ocean University, Zhoushan 316022, China; wangwei1981@zjou.edu.cn (W.W.); hujingyi@zjou.edu.cn (J.H.); xieyh@zjou.edu.cn (Y.X.); jiangdinliang@zjou.edu.cn (D.J.)
[2] School of Naval Architecture Ocean and Civil Engineering, Shanghai Jiaotong University, Shanghai 200240, China
[3] School of Naval Architecture, Ocean and Energy Power Engineering, Wuhan University of Technology, Wuhan 430010, China
* Correspondence: zhaocheng@whut.edu.cn (C.Z.); gxw@zjou.edu.cn (X.G.)

Abstract: Due to the limited availability of land resources, offshore wind turbines have become a crucial technology for the development of deep-water renewable energy. The multi-floating body platform, characterized by its shallow draft and main body located near the sea surface, is prone to significant motion in marine environments. The proper chamfering of the heave plate can effectively enhance its resistance during wave action, thereby improving the stability of the floating platform. The optimal chamfer angle is 35°. Considering the complexity of the floating body's motion response, this study focuses on the damping characteristics of the heave plate with 35° chamfered perforations. Using the NREL 5 MW three-column semi-submersible floating wind turbine platform as the research model, the hydrodynamic characteristics of the floating body with a perforated heave plate are systematically studied through theoretical analysis, numerical simulation, and physical tests. The amplitude of vertical force under various working conditions is measured. Through theoretical analysis, the additional mass coefficient and additional damping coefficient for different working conditions and models are determined. The study confirms that the heave plate with 35° chamfered perforations significantly reduces heave in the multi-floating body.

Keywords: multi-column semi-submersible floating; heave plate; hydrodynamic characteristics; numerical simulation; physical model tests

check for updates

Academic Editors: Juan-Manuel Roldan-Fernandez and Angel G. Gonzalez-Rodriguez

Received: 21 February 2025
Revised: 4 April 2025
Accepted: 5 April 2025
Published: 8 April 2025

Citation: Wang, W.; Hu, J.; Zhao, C.; Xie, Y.; Gong, X.; Jiang, D. Multi-Column Semi-Submersible Floating Body Hydrodynamic Performance Analysis. *Energies* **2025**, *18*, 1884. https://doi.org/10.3390/en18081884

Copyright: © 2025 by the authors. Licensee MDPI, Basel, Switzerland. This article is an open access article distributed under the terms and conditions of the Creative Commons Attribution (CC BY) license (https://creativecommons.org/licenses/by/4.0/).

1. Introduction

With the development of human society, the growing demand for energy coupled with the depletion of fossil fuels has become increasingly prominent, making the development and utilization of renewable energy inevitable. Offshore wind energy is considered one of the most promising technologies in the renewable energy sector [1]. Offshore wind platforms possess characteristics such as vast reserves, non-pollution, renewability, widespread distribution, and low development costs, making them a focal point for the clean energy development of various countries [2]. Since the establishment of the world's first offshore wind farm in Denmark in 1991, offshore wind energy has garnered significant interest from the global energy community [3]. Wind resources are more abundant in deeper waters farther offshore, with wind energy reserves increasing proportionally with greater water depths and distances from the shore. However, the deep-sea environment

presents complex seabed conditions, which floating structures can overcome, making them an optimal choice for deep-sea wind energy. Currently, floating wind power platforms are primarily classified into four conceptual models: barge-type [4,5], tension-legged [6], single-column [7], and semi-submersible [8–10]. Compared to other platform types, semi-submersible platforms offer the advantages of flexible water depth setup, as well as ease of assembly and maintenance.

Suppressing the oscillatory motion of the floating wind turbine platform in the complex marine environment is important to ensure the safe and stable operation of the floating wind turbine. Although the semi-submersible platform has a better application prospect, its main body, due to the large restoring force and restoring moment, partly originating from the mooring of the suspension chain line, will cause a decrease in the power generation efficiency of the wind turbine and may lead to the capsizing of the tower and the platform. Offshore wind platforms are mainly affected by wind and wave current loads, which are mainly manifested as pitching, surge, heave, etc. However, for semi-submersible platforms, heave motion is the most obvious characterization.

Floating wind turbine platforms may be affected by first-order and second-order wave forces, which originate vertically and resonate, leading to fatigue damage to the platform and mooring system [11]. As a key structure affecting the performance of the platform, the heave plate can generate a large number of vortices around the platform during pendulum oscillation, which effectively increases the additional mass and damping of the platform, thus prolonging the period of pendulum oscillation and reducing the intensity of pendulum motion [12–14]. Many researchers have tried to perforate the heave plate to increase the edge length, in an attempt to influence the heave plate damping coefficients through the perforation. The hydrodynamic characteristics of the heave plate are affected by a number of factors [15]. Zhang and Ishihara used the fluid volume method for large eddy simulation to study the hydrodynamic performance of multiple heave plates. The analytical solutions of added mass and drag coefficient are proposed to cover the wide application of heave plates with different shapes [16].

Currently, scholars both domestically and internationally generally reduce the amplitude of platform pitch motions and enhance stability by adding mass to the structure or using pitch damping plates [17]. Han ZL et al. designed a new type of floating wind turbine semi-submersible platform by increasing the added mass, but this method makes the platform heavier, increases costs, and requires larger displacement or increased draft to provide buoyancy [18]. Fan Zhang's model tests studied the impact of the number and type of pitch damping plates on platform pitch motion [19]. Increasing the number of plates and reducing the spacing between them effectively increases the platform's pitch added mass and reduces pitch response. In some cases, perforated plates are more effective than solid plates in reducing pitch response. By adjusting the "perforation area ratio," smaller pitch responses can be achieved. SX Liu et al. conducted forced vibration tests on damping plates with different perforation rates to study their added mass and viscous damping coefficients, comparing the hydrodynamic characteristics of perforated plates with different hole diameters [20].

Most current research focuses on spar-type damping plates, mainly studying 2D perforation shapes and rates, with few systematic studies on chamfered perforated damping plates for semi-submersible platforms. Based on the above research, numerical simulations and physical tests were conducted on chamfered perforated damping plates of the same projection area, examining their hydrodynamic performance under different motion cycles and amplitudes in still water.

Wang W et al. [21] investigated the effect of perforated chamfer on the hydrodynamic performance of heave plate. The reducing plate of a DeepCwind floating wind turbine

platform with a capacity of 5 MW was used as the study object. The results show that a proper chamfer (the optimum chamfer is 35°) can effectively increase the drag force of the heave plate and improve the stability of the heave plate. In this study, this type of damping plate was mounted on the platform base, and numerical simulations and model tests with vertical buoyancy cylinders were conducted to further verify the feasibility and damping effect of this type of damping plate.

This paper focuses on the 5 WM multi-column semi-submersible floating body. It uses numerical simulation and physical testing to examine how the vibration period and movement amplitude change with variations in the pendulum plate damping coefficient and additional mass coefficient. The paper analyzes how chamfered openings on the overall platform foundation affect the hydrodynamic performance.

The innovativeness of this paper is mainly reflected in the following:

(1) Through studying various types of damping mechanisms, a novel chamfered perforated damping plate device is proposed, which effectively improves the motion characteristics of multi-column semi-submersible floating bodies for offshore wind platforms.
(2) A dual-control experimental driving device is designed, and a series of model tests on a three-column floating body are conducted to investigate the hydrodynamic damping performance and the sensitivity of key parameters of the chamfered perforated design, confirming its effectiveness.
(3) A series of numerical simulations are performed and compared with experimental results, yielding the optimal chamfered perforated parameter combination. Under regular wave conditions, the vertical motion damping effect of the floating body can reach 5%, demonstrating practical application potential.

2. Theoretical Background

The Reynolds number is one of the most commonly used dimensionless parameters in fluid dynamics and serves as a criterion for characterizing the effects of viscosity. It is one of the fundamental dimensionless numbers in fluid dynamics and is closely related to many physical phenomena in viscous fluids, representing the ratio of inertial forces to viscous forces [22]. The Keulegan–Carpenter number is another important dimensionless quantity, which characterizes the magnitude of an object's motion within a flow field.

The hydrodynamic performance of the heave plate in the pendant oscillation process mainly depends on the two dimensionless parameters, KC and R_e; the calculation of KC and R_e is shown in Equations (1) and (2) [23].

$$KC = \frac{v_O T}{L} = \frac{2\pi A}{L} \tag{1}$$

$$R_e = \frac{A\omega L}{v} \tag{2}$$

where v_O is the velocity amplitude, T is the period of vibration, L is the characteristic length of the heave plate (diameter of the heave plate D_d), A is the amplitude of the simple harmonic motion, and v is the kinematic viscosity coefficient of the fluid.

Therefore, this paper investigates the variation in the hydrodynamic coefficients of a three-column floating body with 35° chamfered perforations to reduce heave plates as the number of KC increases.

Due to the small wave steepness under linear sea conditions, wave breaking is unlikely to occur. Therefore, linear theory can be used to analyze and predict the wave loads and induced motions on vibrating floaters to a large extent. An important feature of linear theory is that it allows for the superposition of responses to regular waves with different

wave heights, wavelengths, and directions to obtain the response under irregular waves. Thus, it is sufficient to analyze the wave loads and motion responses of floating structures under sinusoidal regular waves with small wave steepness.

For the numerical simulation of semi-submersible floats with columns, their displacements are shown in Equation (3), and their forces can be calculated by Equation (4) [23]:

$$z(t) = A\sin(\omega t), \tag{3}$$

$$F_H(t) = -A_{33}\ddot{z} - B_{33}\dot{z} = -F_{flu} + C_{33}z \tag{4}$$

C_{33} is the static restoring force coefficient during the oscillatory motion, $C_{33} = \rho g A_w$; A_w is the waterline surface area of the single-column floating body model during the oscillatory motion, $A_w = \frac{\pi D^2}{4}$; D is the diameter of the column.

A_{33} and B_{33} can be directly transformed by Equation (4):

$$A_{33} = -\frac{\int_t^{t+T} F_H(t)\cdot\ddot{z}(t)dt}{\int_t^{t+T}\ddot{z}^2(t)dt}, \tag{5}$$

$$B_{33} = -\frac{\int_t^{t+T} F_H(t)\cdot\dot{z}(t)dt}{\int_t^{t+T}\dot{z}^2(t)dt}, \tag{6}$$

Thereby, the additional mass coefficient A'_{33} and the damping coefficient B'_{33} are obtained, and the specific expressions for A'_{33} and B'_{33} are given in Equations (7) and (8) [23].

$$A'_{33} = \frac{A_{33}}{A_{33,th}} = -\frac{3F_0\cos(\varphi)}{A\omega^2\rho D_d^3} = 3C_m, \tag{7}$$

$$B'_{33} = \frac{B_{33}}{\omega A_{33,th}} = \frac{3F_0\sin(\varphi)}{A\omega^2\rho D_d^3} = \frac{4A}{\pi D_d}C_d, \tag{8}$$

For the physical test of the forced vibration of a floating body with a column, its displacement is shown in Equation (3), and its force can be calculated by using Equation (9) [23]:

$$F_H(t) = -A_{33}\ddot{z} - B_{33}\dot{z} = -F_{ext} + M\ddot{z} + C_{33}z \tag{9}$$

A is the amplitude of vibration of a single-column floating body; A_{33} is the aditional mass of the the single column floater; B_{33} is the equivalent linear damping; F_{ext} is measuring force; M is the mass of the single column float; C_{33} is the static restoring force coefficient during the oscillatory motion, $C_{33} = \rho g A_w$; A_w is the waterline surface area of the single-column floating body model during the oscillatory motion, $A_w = \frac{\pi D^2}{4}$; D is the diameter of the column.

A_{33} and B_{33} can be directly transformed from Equation (4) to obtain Equations (5) and (6), which in turn obtains the additional mass coefficient A'_{33} and the damping coefficient B'_{33}, and the specific expressions for A'_{33} and B'_{33} are shown in Equations (7) and (8).

For the three-column float, M in the above equation is the total weight of the three-column float, $A_{33,th} = \rho D_d^3$; A_w is the waterline surface area of the three-float model during the oscillatory motions, $A_w = \frac{3\pi D^2}{4} + S$, and S is the waterline surface area of the central column.

This paper investigates the variation of vertical force amplitude, additional mass coefficient A'_{33}, and damping coefficient B'_{33} with the increase of KC for multi-column semi-submersible floats with 35° chamfered perforations heave plate and without perforations heave plate under different working conditions.

According to similarity theory, models and prototypes must satisfy geometric similarity, kinematic similarity, and dynamic similarity. However, it is impossible to meet all three simultaneously.

In marine engineering model testing, the effects of viscosity are typically neglected or abandoned, maintaining equal Froude and Strouhal numbers between the prototype and the model, thus satisfying gravity and inertial force similarity.

$$\frac{v_s}{\sqrt{gL_s}} = \frac{v_m}{\sqrt{gL_m}} \tag{10}$$

$$\frac{v_s T_s}{L_s} = \frac{v_m T_m}{L_m} \tag{11}$$

where v is the velocity amplitude, T is the period of vibration, L is the characteristic length of the heave plate (diameter of the heave plate D_d), and g is the acceleration due to gravity.

Failure to achieve complete dynamic similarity may lead to deviations in physical phenomena, inaccurate wave load and response predictions, and violations of similarity criteria. Complete dynamic similarity is difficult to achieve in practice, especially in cases involving complex fluid–structure interactions. Typically, we optimize the model experiments and extrapolation process through a reasonable compromise of different similarities, combining numerical simulations and experimental data to minimize errors and improve the reliability of the results.

3. Model Experiment

This study uses the NREL 5 MW three-column semi-submersible floating wind turbine platform as the research model, featuring a three-column floating body structure for the floating foundation. The specific dimensions are presented in Table 1.

Table 1. The dimension of the three-column floating bodies.

Projects	Dimension (m)	Projects	Dimension (m)
Platform base draft	20	Damping cylinder height	6
Waterline height from top	10	Float draft below the waterline	14
Float height above the waterline	12	Diameter of float	12
Height of float	26	Damping cylinder diameter	24

Due to the width of the experimental tank being 6 m, the designed experimental device motor can provide a maximum cycle of 2 s and a maximum motion amplitude of 0.16 m. The relevant working conditions, when converted based on the Froude number and Strouhal number, indicate that a scale ratio of $\lambda = 60$ is the largest feasible option that satisfies geometric similarity. A larger model would exceed the device's limits, while a smaller model may not accurately simulate the fluid behavior in the actual structure, leading to test results that do not match the real situation.

To keep the same draught, the weight is adjusted by adding ballast to satisfy the similarity requirement. The specific dimensions of the oscillating plate model are shown in Table 2.

Table 2. The dimension of heave plate.

Projects	Physical Dimension (m)	Molded Dimension (m)
Diameter of heave plate	24	0.4
Height of heave pl ate	6	0.1

The test device generates reciprocating motion by controlling the motor, and the slider can be driven by the motor to produce cyclic motion in the vertical direction along the sliding rail. A steel pipe with a length of 1 m is used to pass through the center of the pendulum plate and fixed with bolts, and the top of the pipe is fixed with the slider, so that the pendulum plate together with the steel pipe can produce cyclic motion along with the slider in the vertical direction; the steel pipe is cut off close to the slider and installed with the six-dimensional force sensor to measure the force on the system in the process of the test; a displacement sensor is installed to measure the vertical displacement during the test of the pendulum plate to verify the consistency with the given motion process. The steel tube is truncated near the slider, and a six-dimensional force transducer is installed to measure the force exerted on the system during the test; a displacement transducer is installed to measure the vertical displacement of the pendant plate during the test, which is used to verify whether the movement of the slider is the same as the given movement process; since the pendant plate and the slider are already cemented together, the displacement of the slider in the vertical direction is the vertical displacement of the heave plate. Figure 1 shows the sketch of the device.

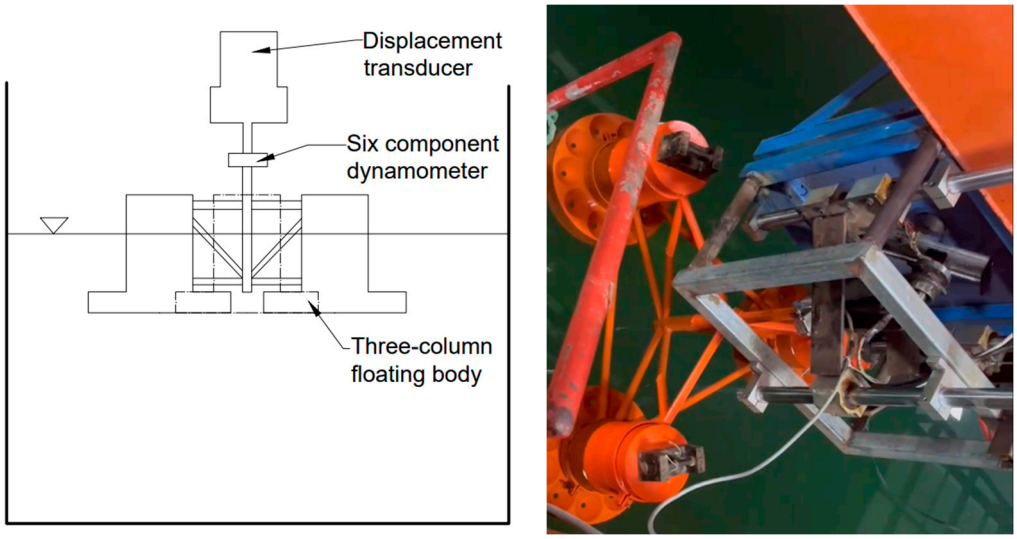

Figure 1. Site layout and installation diagram: (**a**) Device sketch; (**b**) On-site photo.

A Net FT six-dimensional force transducer with a range of 0–200 N and an accuracy of ±0.5% FS was used for the experiments; the data were sampled at 500 Hz with a signal-to-noise ratio of >60 dB. The water temperature was controlled at 20 ± 0.5 °C to minimize the effect of fluctuations in the fluid properties. In the forced vibration test, the test equipment is driven by a motor to perform periodic motion. A six-dimensional force sensor is mounted on top of the damping device and moves together with the drive mechanism. The sensor has high sampling frequencies, and the collected results correspond to specific time points, ensuring the synchronization of the force and displacement curves.

The test steps are as follows:

1. Install and fix the test device with dual control functions for frequency and phase on the trailer.
2. Connect the six-dimensional force sensor to the test device using a connector, linking it to the single-column floating body.
3. Move the trailer to the center of the water tank to minimize the wall effect during the test.

4. Start the test device and adjust the motion cycle and amplitude through control software, then conduct tests under different conditions.
5. After completing the model test, repeat steps (1) to (4) to test another model.

Each test is repeated 3–4 times. After excluding data with obvious measurement issues, the remaining clear data are averaged.

4. Numerical Simulations

In this study, a CFD numerical simulation was conducted for the multi-column semi-submersible wind turbine platform; the numerical simulation of calm water was carried out using the STAR-CCM+ 2210 (17.06.007-R8) software.

In the numerical simulation process, the RANS turbulence, K-Epsilon turbulence, separated flow, constant density, implicit unsteady, realizable K-Epsilon two-layer, and gradient turbulence models were used. The K-Epsilon turbulence model has advantages such as high numerical stability and accurate pressure gradients, making it the most widely used turbulence model currently.

The numerical simulation employs a moving mesh method using overlapping grids. The required motion frequency ω and amplitude A for the forced vibration of the heaving plate are set, forming the displacement formula for the heaving motion of the plate: $z = A\sin(\omega t)$. In the motion module of STAR-CCM+, translational motion is created and added to the overlapping region. The heaving velocity in the z-axis direction is controlled by the field function ($[0.0,\ 0.0,\ \$\{A\} * \$\{\omega\} * \cos(\$\{\omega\} * \$\{Time\})]$), which determines the vertical motion velocity in the static calculation domain.

A rectangular computational domain is used, and the coordinate origin is located at the center of the bottom line of the three-column float pendant swing plate, and the center of the bottom line of the three-column float is located at the center of the whole computational domain. In the setting of boundary conditions, the three-column floating body is set as a smooth wall; the left side of the computational domain for the velocity inlet, the speed of hydrostatic velocity is 0 m/s; the right side of the computational domain for the pressure outlet, the pressure of hydrostatic pressure; the computational domain of the upper side of the velocity inlet, the speed of hydrostatic velocity; the computational domain of the other surfaces for the symmetry of the plane, specifically shown in Figure 2.

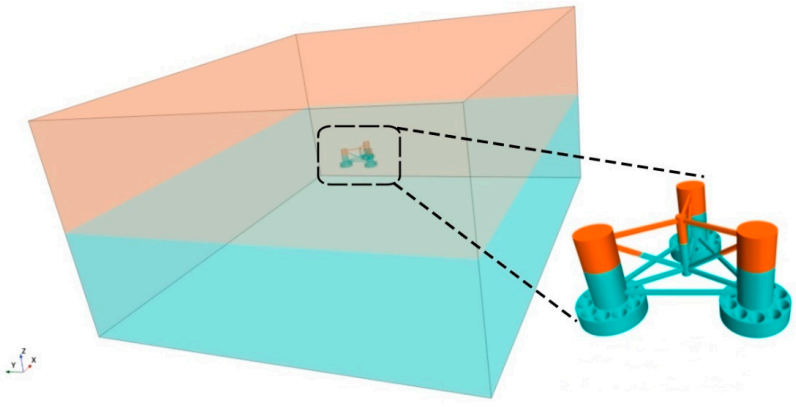

Figure 2. Schematic boundary conditions and mesh for numerical simulation.

The numerical simulation adopts the method of moving grid, using the overlapping grid to create the translational motion in the motion module, the motion of the three-column float is set as a single-degree-of-freedom, z-direction motion, and the hydrodynamic force on the three-column float is tracked and measured after setting up the different working conditions.

In the research process, reference to the actual sea conditions, and test equipment, according to the equality of Froude Number, each model is set up with five motion cycles and five motion amplitudes, and there are two models and 50 working conditions, shown in Table 3.

Table 3. Calculation cases of three-column floating body.

Models	Motion Periods (s)	Motion Amplitude (m)
With 35° chamfered perforations Without perforations	2.5, 5, 7.5, 10, 12.5	0.03, 0.06, 0.09, 0.12, 0.15

In this paper, based on the viscidity theory, numerical simulation and experimental methods are given to solve the interaction between waves and the open chamfered oscillation reduction device, and the above methods are applied to solve the hydrodynamic characteristic problem of the oscillation reduction device. The research object in the paper is taken from the 5 MW three-column semi-submersible floating wind turbine platform of the National Renewable Energy Laboratory (NREL) in the United States of America, and the modelling dimensions are the same as the dimensions of the wind turbine platform. Numerical simulations were used to investigate the hydrodynamic performance of the three-column floating body with 35° chamfered perforations in the heave plate and without perforations with different motion periods and motion amplitudes. The specific dimensions of the models are shown in Table 4. The numerical simulation and physical experiment in this paper are calculated by the scale model.

Table 4. Data sheet of the numerical simulation model.

Projects	Numerical Simulation (m)	Test Model (m)
Diameter of heave plate	24	0.4
Diameter of the float	12	0.2
Number of columns	3	3
Perforation Ratio	44.12%	44.12%

The three-column floating body model is shown in Figure 3.

When performing numerical simulation, a too small computational domain or too large mesh will give the numerical simulation a large error, and a too large computational domain and too precise mesh will make the computation time too long and increase the cost of numerical simulation, so it is necessary to validate the mesh convergence of the numerical simulation: the computational domains of five different sizes are computed, and the dimensions of the computational domains are: 10 m × 8 m × 3.13 m, 11 m × 9 m × 4.13 m, 12 m × 10 m × 5.13 m, 13 m × 11 m × 6.13 m, and 14 m × 12 m × 7.13 m, respectively. 4.13 m, 12 m × 10 m × 5.13 m, 13 m × 11 m × 6.13 m, and 14 m × 12 m × 7.13 m.

Figure 4 shows that the amplitudes of the vertical force of the three-column floating body move closer to each other as the computational domain increases.

Considering the number of grids, computational time consumption, and the reliability of the results, the computational domain of 13 m × 11 m × 6.13 m was selected for the relevant simulations. Grid validation was carried out for five grid quantities, namely 871,066, 980,427, 1,334,955, 2,671,392, and 5,799,001.

Figure 4 represents the amplitude of the vertical force of the three-column floating body under different cell numbers, which changes continuously with the increase in the number of grids and finally remains relatively stable, and the amplitude is basically stable when the number of grids is 2,671,392.

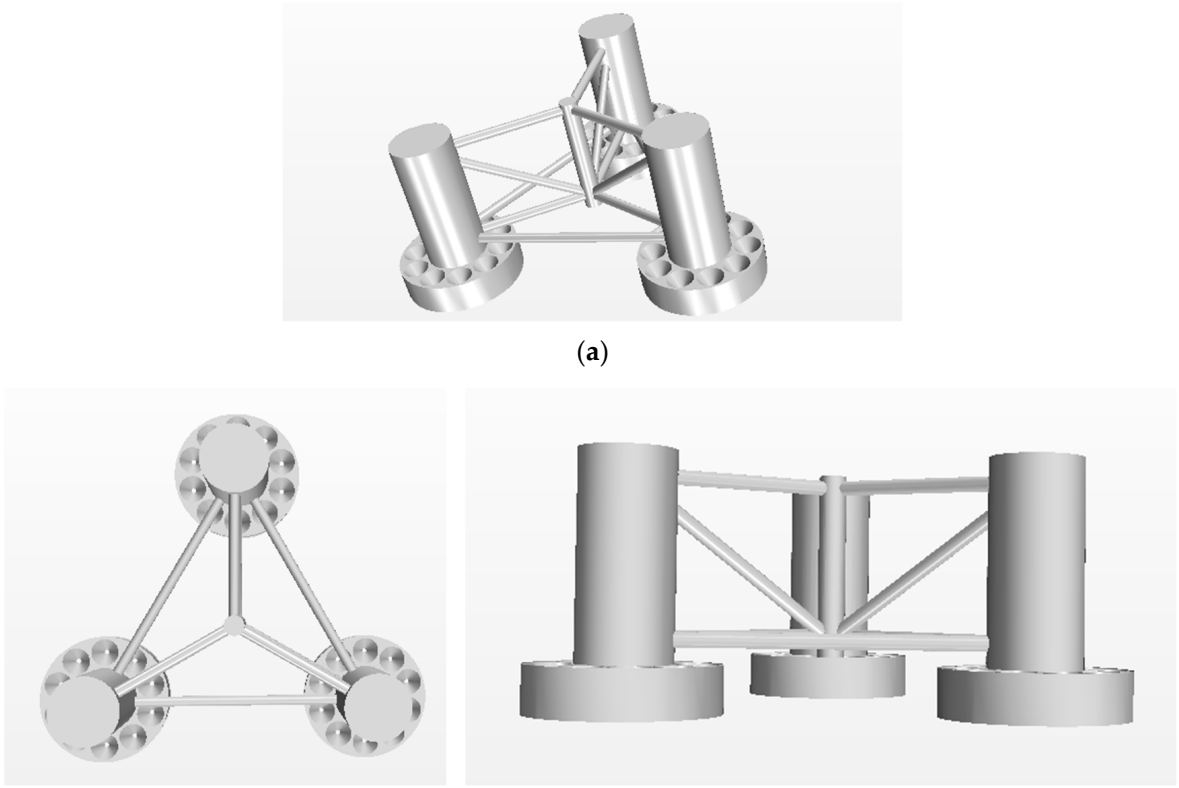

(**a**)

(**b**) (**c**)

Figure 3. Simplified model of numerical simulation: (**a**) Oblique view; (**b**) Top view; (**c**) Front view.

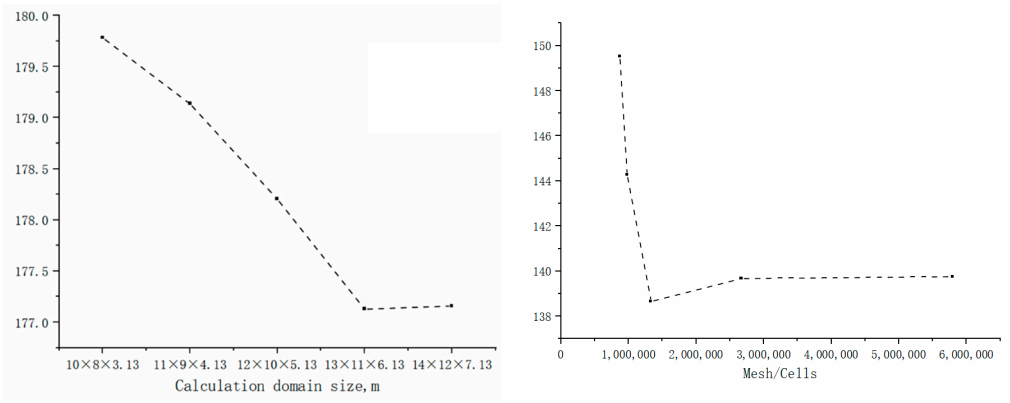

(**a**) (**b**)

Figure 4. Grid Adaptation Findings: (**a**) Vertical force amplitude of three-column floating bodies in different calculation domains; (**b**) Vertical force amplitude of three-column floating bodies in different numbers of meshes.

Figure 4 shows that when the computational domain reaches 13 m × 11 m × 6.13 m and 14 m × 12 m × 7.13 m, the numerical results are nearly identical, with a difference of only 0.03127 or 0.0177%, as shown in Table 5. When the grid numbers are 1,334,955, 2,671,392, and 5,799,001, the differences between the three are very small. The difference between the grid number of 2,671,392 and the previous and subsequent two schemes is 1.01245 and 0.08296, corresponding to a difference of 0.7302% and 0.0594%, respectively.

Table 5. Calculate the relative change in domain size.

Calculation Domain Size	10 × 8 × 3.13	11 × 9 × 4.13	12 × 10 × 5.13	13 × 11 × 6.13	14 × 12 × 7.13
Force (N)	179.78109	179.13518	178.20363	177.12746	177.15873
Relative change (%)	-	−0.359%	−0.520%	−0.604%	0.018%

Grid convergence is determined by the criterion that the difference between the vertical force amplitudes of two adjacent grids is less than 1%. As shown in Table 6, when the number of grids increases from 2,671,392 to 5,799,001, the vertical force amplitude changes by only 0.04%, which satisfies the engineering convergence criterion and is far lower than the threshold value, which proves that the grid independence is established.

Table 6. Relative change in mesh density.

Mesh	871,066	980,427	1,334,955	2,671,392	5,799,001
Force (N)	149.51833	144.27068	138.65513	139.66758	139.75054
Relative change (%)	-	−3.510%	−3.892%	0.730%	0.059%

Considering computational efficiency and computational accuracy, a computational domain of 13 m × 11 m × 6.13 m with a grid number of 2,671,392 was finally selected for the relevant numerical analyses, and the grid layout is shown in Figure 5.

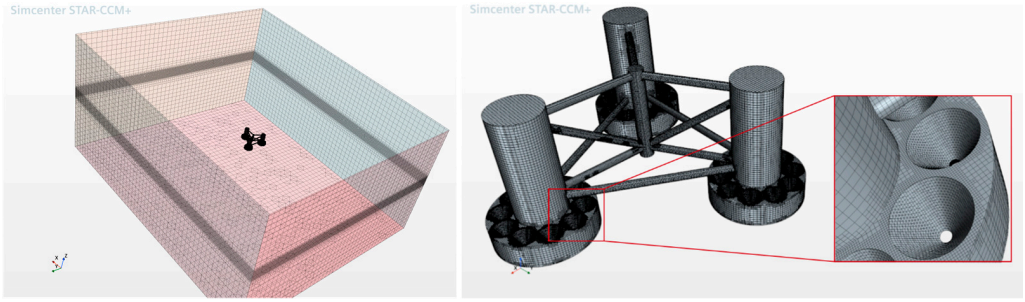

(**a**) (**b**)

Figure 5. Schematic diagram of the numerical simulation grid of three-column floating bodies: (**a**) Compute Domain Model (CDM); (**b**) Partial schematic of the model.

5. Results and Discussion

5.1. Analysis of the Experiment

This section primarily investigates the force acting on a three-column floating body with a 35° chamfered perforated heave plate under different motion amplitudes and periods. When the period reaches 12.5 s, the trailer platform generates significant vibrations during the test, leading to unreliable data. Therefore, results from tests with periods of 5, 7.5, and 10 s are processed to analyze the changes in the test results in the time domain. A certain amount of noise is present, which is reduced using low-pass filtering. Fourier transforms are applied to obtain the dominant frequency, and the low-pass filtering process ensures that the results are confined to the main frequency range, generating the time-domain curve of periodic changes. Figure 6 illustrates the changes before and after filtering. From the stable periodic curve, the amplitude of the vertical force on the three-column floating body under various working conditions is extracted, and the results are shown in Figure 7. Figure 6 illustrates the changes before and after filtering.

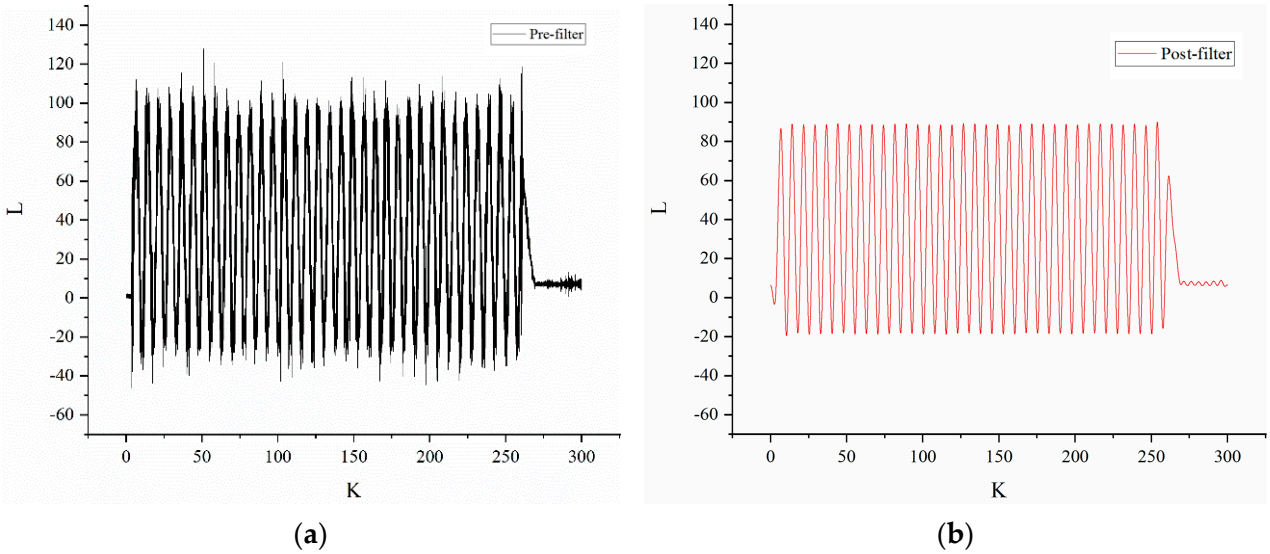

Figure 6. Comparison chart before and after filtering: (**a**) pre-filter; (**b**) post-filter.

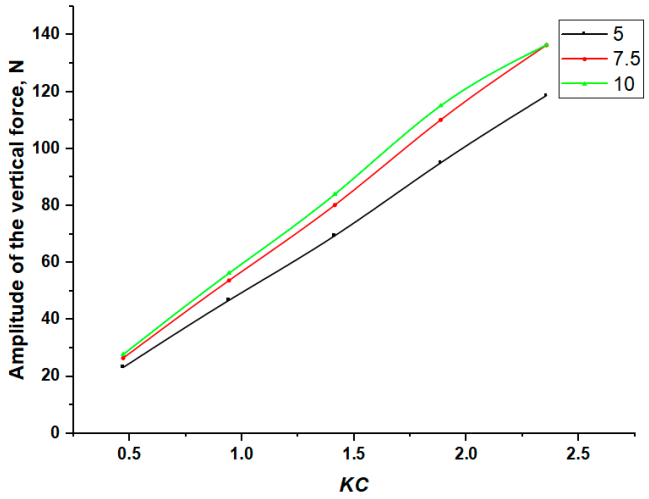

Figure 7. The relationship between the amplitude of vertical force and the motion amplitude of three-column floating bodies.

The results in Figure 7 show that the amplitude of the vertical force on the three-column floating body increases with the increase KC.

Using Equations (5) and (6), the added mass coefficient A'_{33} and damping coefficient B'_{33} are obtained for the three-column floating body under different operating conditions for the 35° opening case, and the variation curves of the hydrodynamic coefficient of the three-column floating body with the number of KC ($KC = 2\pi A/L$) are obtained by summarising and comparing them, and the results are shown in Figure 4.

From Figure 8, it can be seen that the damping coefficient of the three-column floating body increases with the increase in the number of KC and the additional mass coefficient decreases with the increase in the number of KC when the period is 5, 7.5, and 10 s. The damping coefficient of the three-column floating body increases with the increase in the number of KC. The trend is consistent with the numerical simulation results.

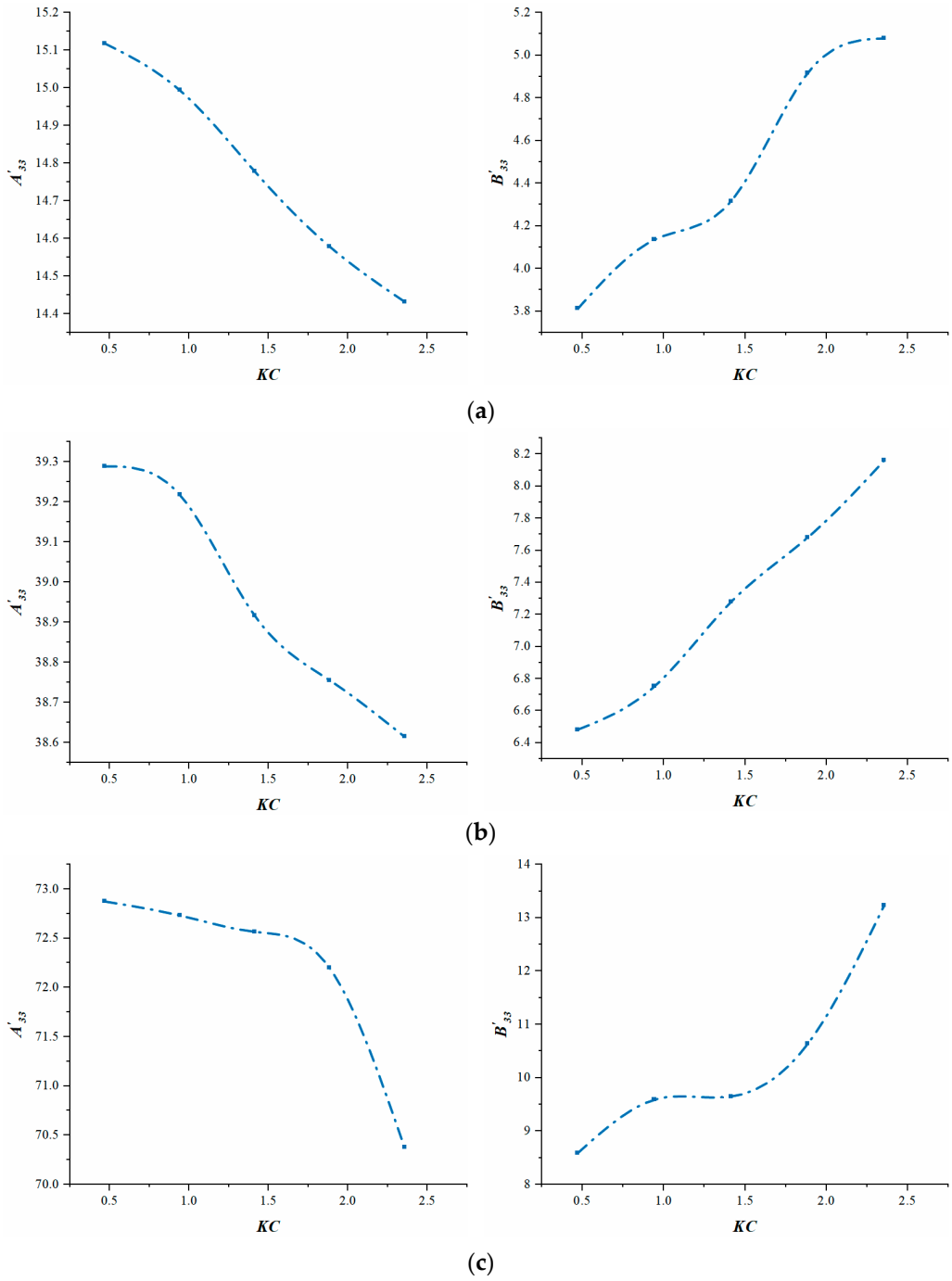

Figure 8. The results of added mass coefficient and damping coefficient of three-column floating bodies without perforations: (**a**) T = 7.5 s; (**b**) T = 10 s; (**c**) T = 12.5 s.

5.2. Analysis of Numerical Simulation Results

The numerical simulation adopts the VOF hydrostatic flow field and uses the translational motion field function to achieve the up and down translation of the model to simulate the forced vibration of the floating platform in hydrostatic water. The three-column semi-submersible platform with a 35° chamfered open plate and a three-column semi-submersible platform without an open plate are simulated under different working conditions. In the STARCCM+ 2210 (17.06.007-R8) software, the vertical force during the float translation is monitored, and the amplitude of the vertical force in the stable section of the curve is collected under different working conditions. The data curves are shown in Figures 9–13. Grid convergence is determined by the criterion that the difference between

the vertical force amplitudes of two adjacent grids is less than 1%. As shown in Table 5, when the number of grids increases from 2,671,392 to 5,799,001, the vertical force amplitude changes by only 0.04%, which satisfies the engineering convergence criterion and is far lower than the threshold value, which proves that the grid independence is established.

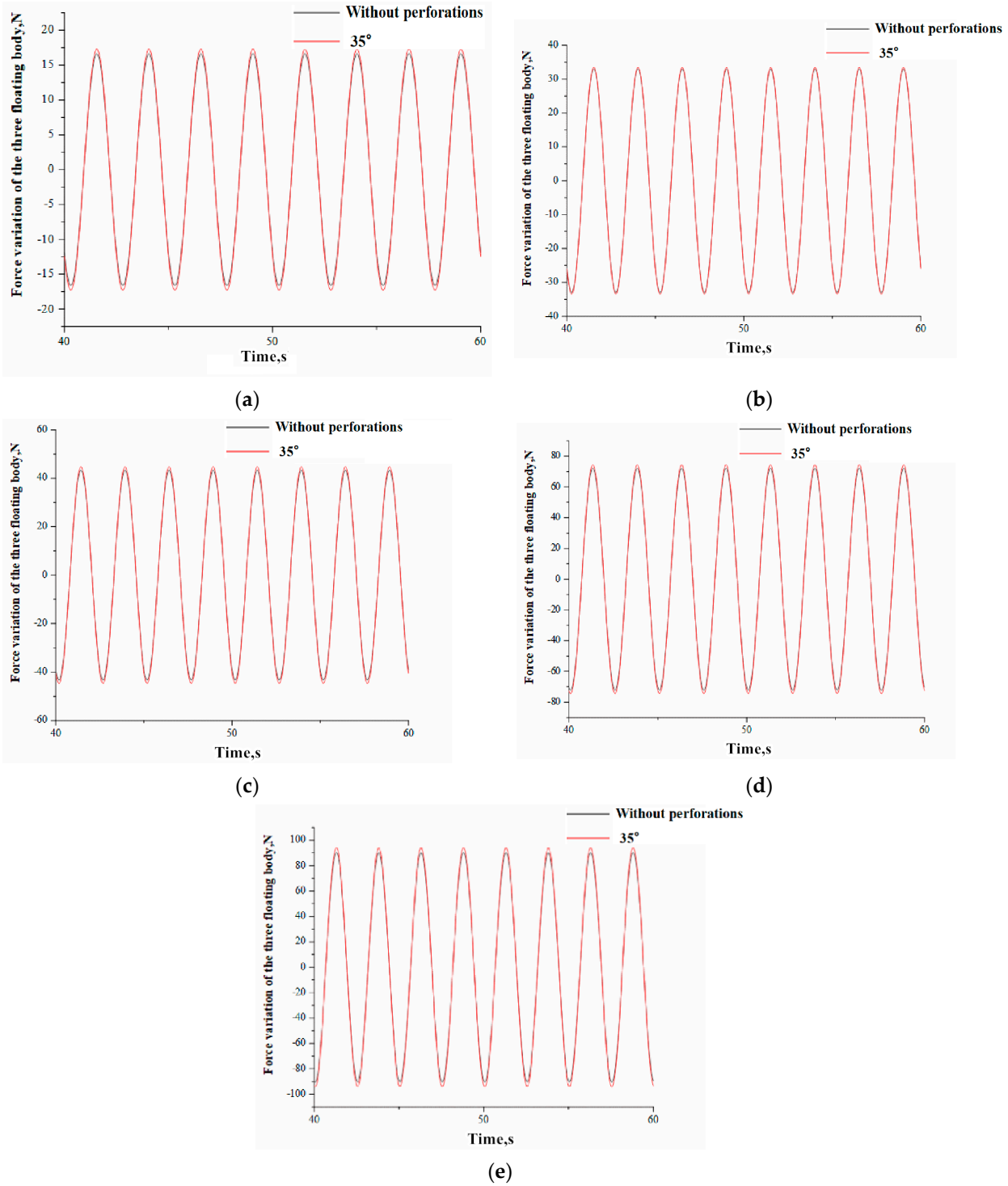

Figure 9. The time history curves of the force of a three-column floating body under different motion amplitudes (T = 2.5 s): (**a**) A = 0.03 m; (**b**) A = 0.06 m; (**c**) A = 0.09 m; (**d**) A = 0.12 m; (**e**) A = 0.15 m.

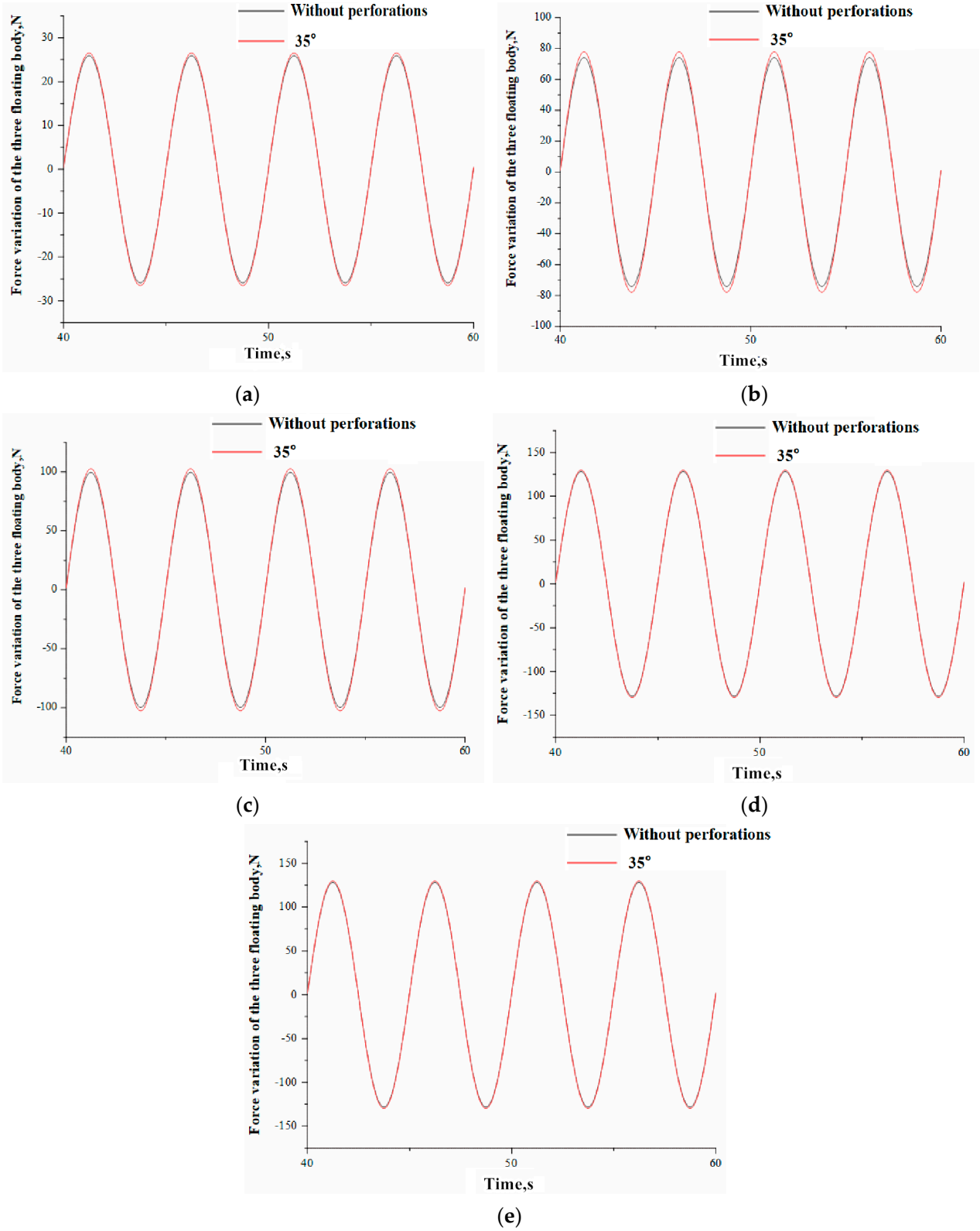

Figure 10. The time history curves of the force of a three-column floating body under different motion amplitudes (T = 5.0 s): (**a**) A = 0.03 m; (**b**) A = 0.06 m; (**c**) A = 0.09 m; (**d**) A = 0.12 m; (**e**) A = 0.15 m.

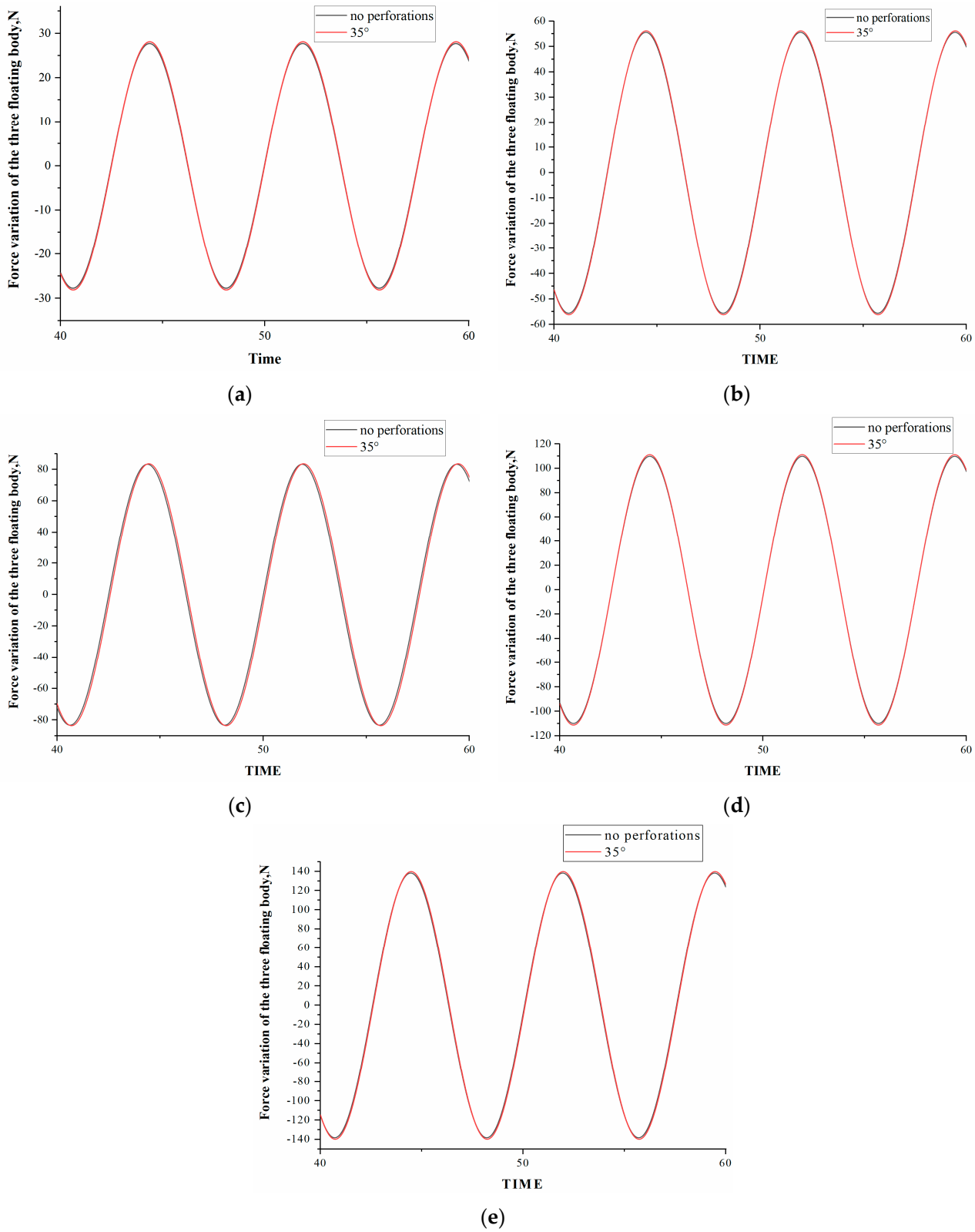

Figure 11. The time history curves of the force of a three-column floating body under different motion amplitude (T = 7.5 s): (**a**) A = 0.03 m; (**b**) A = 0.06 m; (**c**) A = 0.09 m; (**d**) A = 0.12 m; (**e**) A = 0.15 m.

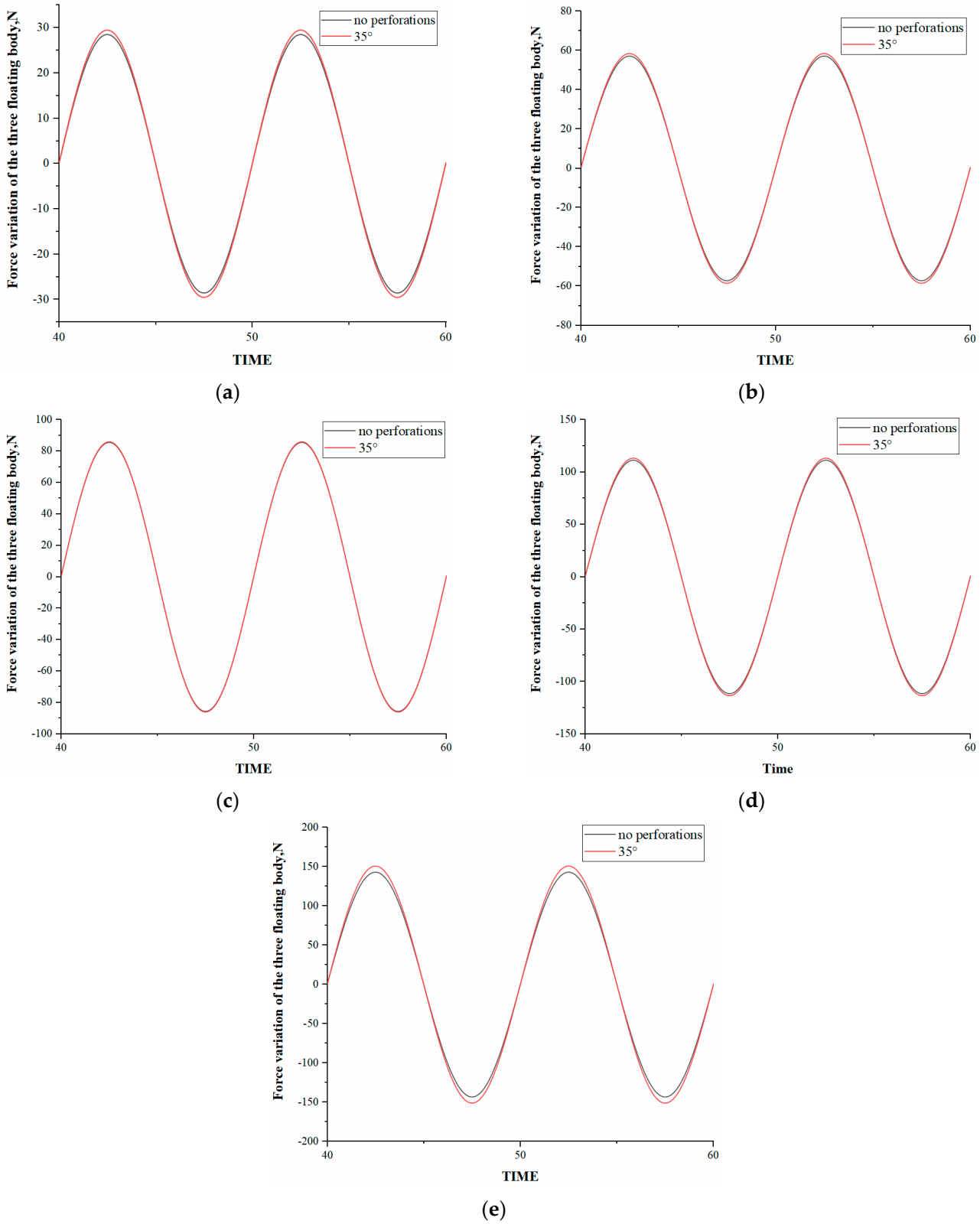

Figure 12. The time history curves of the force of three-column floating body under different motion a mplitude (T = 10 s): (**a**) A = 0.03 m; (**b**) A = 0.06 m; (**c**) A = 0.09 m; (**d**) A = 0.12 m; (**e**) A = 0.15 m.

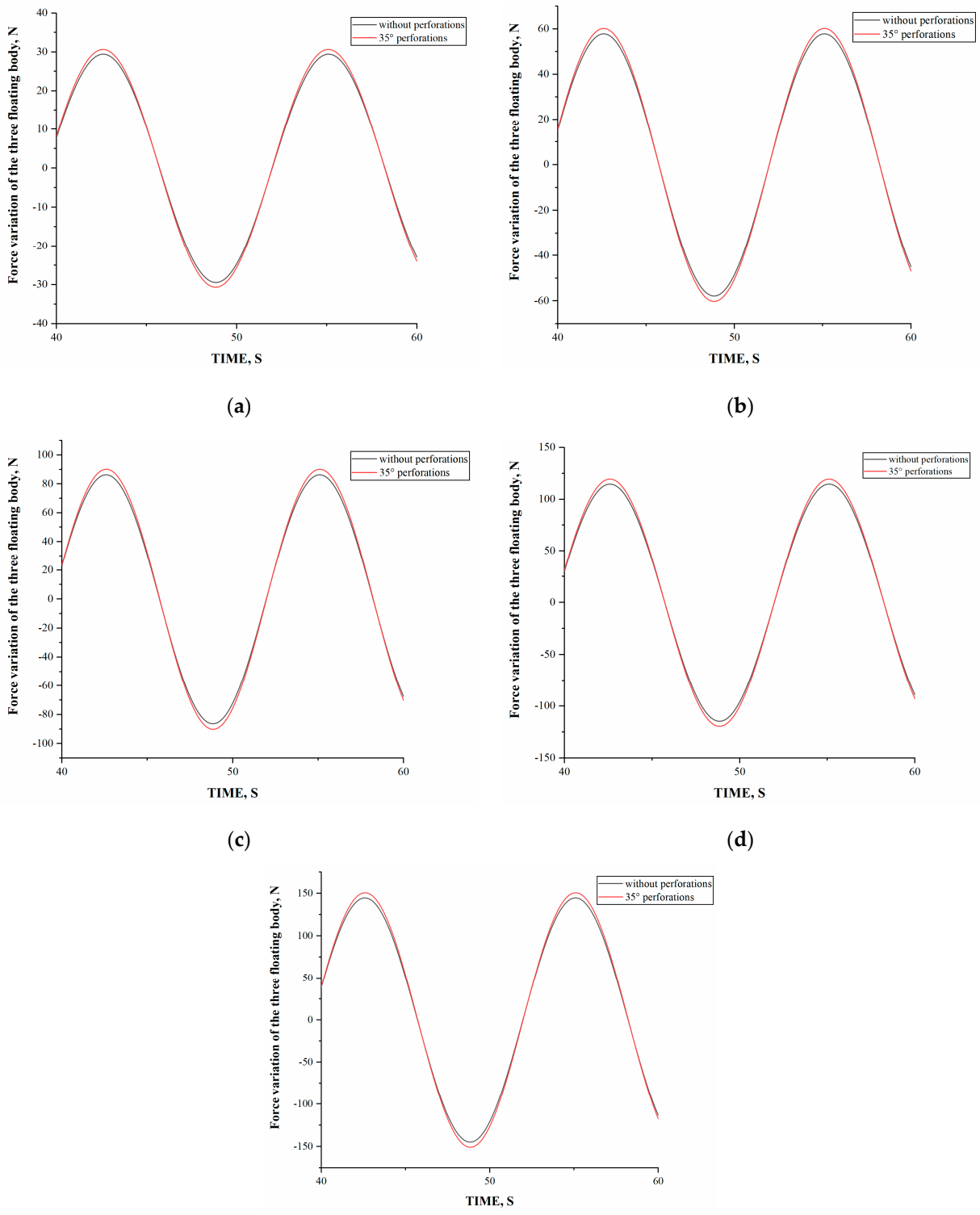

Figure 13. The time history curves of the force of a three-column floating body under different motion amplitudes (T = 12.5 s): (**a**) A = 0.03 m; (**b**) A = 0.06 m; (**c**) A = 0.09 m; (**d**) A = 0.12 m; (**e**) A = 0.15 m.

The amplitude of the motion and the period of the different working conditions are shown by the number of KC ($KC = 2\pi A/D_d$) and the amplitude and period of the motion under different working conditions. Figure 14 shows the variation trend of vertical force amplitude with KC number for different cycles.

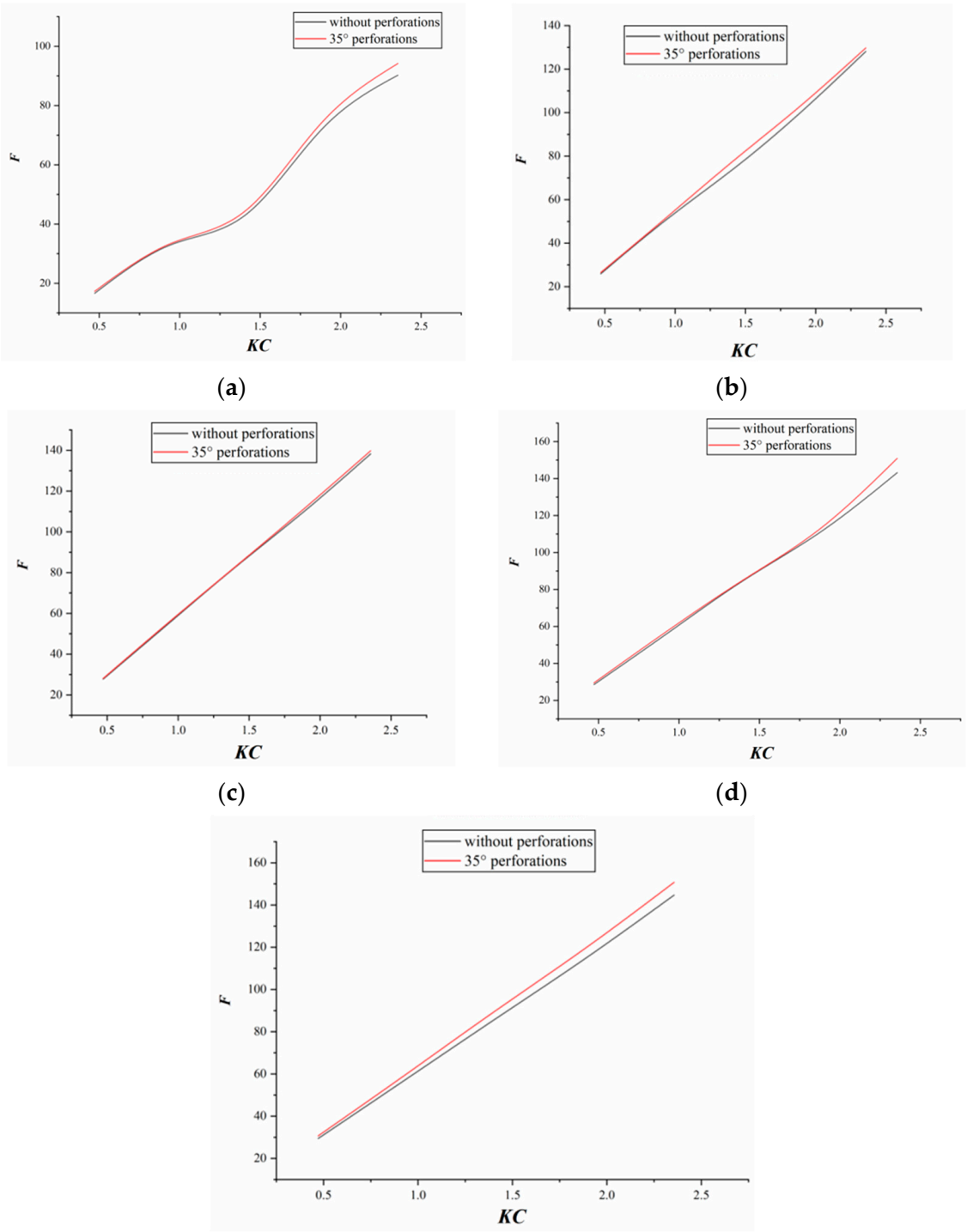

Figure 14. The results of the amplitude of the vertical force under 35° chamfer and without perforations: (**a**) T = 2.5 s; (**b**) T = 5.0 s; (**c**) T = 7.5 s; (**d**) T = 10 s; (**e**) T = 12.5 s.

As shown in Figure 14, the amplitude of the vertical force on the three-column floating body with 35° chamfered perforations is greater than that without perforations for the same period of motion and the same amplitude of motion. Figure 14 indicate that the amplitude of the vertical force on the three-column floating body increases with the increase in the number of *KC* for the same period and that, for the same motion amplitude, the amplitude of the vertical force increases with the increase in the motion period first in a basically linear enhancement relationship.

Tables 7–11 show the forces acting on the model without perforations and the model with 35° chamfered perforations at different KC numbers. The data indicate that, at the same KC number, the model with 35° chamfered perforations experiences higher forces. This suggests that under real sea conditions, the platform's heave motion will generate greater resistance, thereby reducing the heave amplitude.

Table 7. Force amplitude increases between No perforations and 35° perforations (T = 2.5 s).

Factor	KC	No Perforations, N	35° Perforations, N	Increase
	0.47124	16.60277	17.28104	4.09%
	0.94248	32.94793	33.39873	1.37%
F	1.41372	43.26678	44.6997	3.31%
	1.88496	72.09508	74.37175	3.16%
	2.35619	90.25761	94.19257	4.36%

Table 8. Force amplitude increases between No perforations and 35° perforations (T = 5.0 s).

Factor	KC	No Perforations, N	35° Perforations, N	Increase
	0.47124	25.92739	26.53887	2.36%
	0.94248	51.0575	52.05438	1.95%
F	1.41372	74.12695	77.8411	5.01%
	1.88496	99.64354	102.72114	3.09%
	2.35619	128.12347	129.74676	1.27%

Table 9. Force amplitude increases between No perforations and 35° perforations (T = 7.5 s).

Factor	KC	No Perforations, N	35° Perforations, N	Increase
	0.47124	27.71179	28.11141	1.44%
	0.94248	55.5883	56.18021	1.06%
F	1.41372	83.27465	83.59649	0.39%
	1.88496	109.85856	111.20646	1.23%
	2.35619	138.26485	139.78864	1.10%

Table 10. Force amplitude increases between No perforations and 35° perforations (T = 10 s).

Factor	KC	No Perforations, N	35° Perforations, N	Increase
	0.47124	28.52062	29.49162	3.40%
	0.94248	57.17813	58.4825	2.28%
F	1.41372	85.57858	85.99384	0.49%
	1.88496	111.42779	113.36789	1.74%
	2.35619	143.17334	150.92886	5.42%

Table 11. Force amplitude increases between No perforations and 35° perforations (T = 12.5 s).

Factor	KC	No Perforations, N	35° Perforations, N	Increase
	0.47124	29.43808	30.656	4.14%
	0.94248	57.85113	60.22865	4.11%
F	1.41372	86.31472	90.14106	4.43%
	1.88496	114.65153	119.48733	4.22%
	2.35619	144.72441	150.76681	4.18%

After obtaining the vertical force, using Equations (3)–(6), the additional mass coefficients and damping coefficients of the three-column floating body for the two cases are obtained with the increase in KC by the same KC ($KC = 2\pi A / D_d$) reflecting the motion amplitude and period of different working conditions; the results are shown in Figure 15.

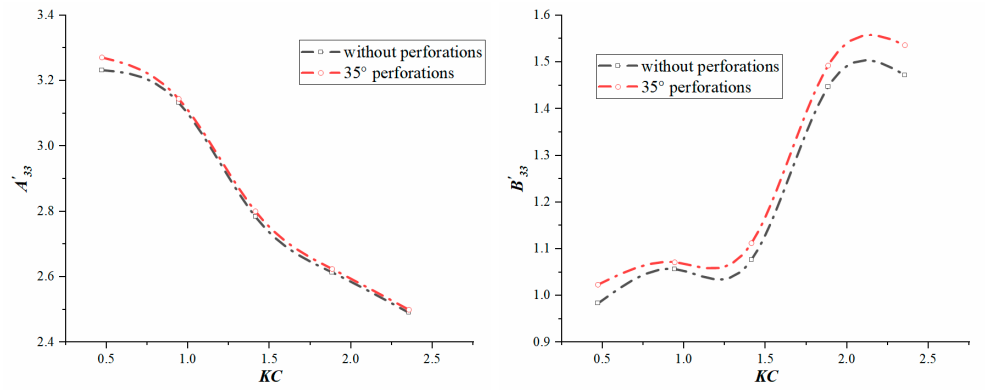

(**a**)

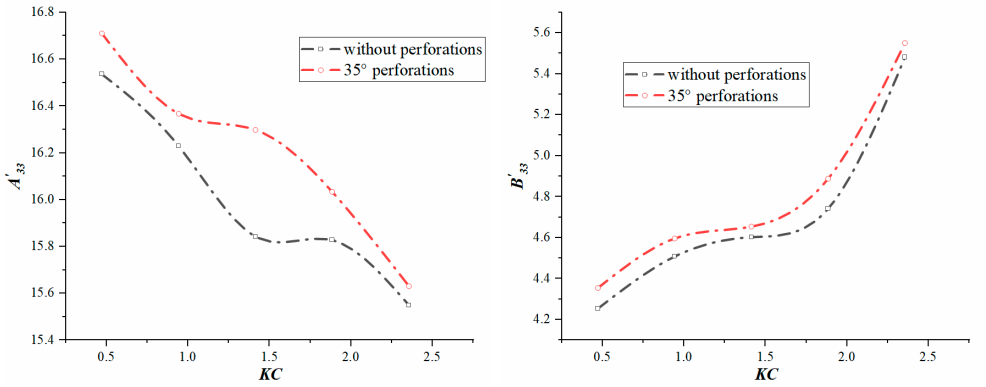

(**b**)

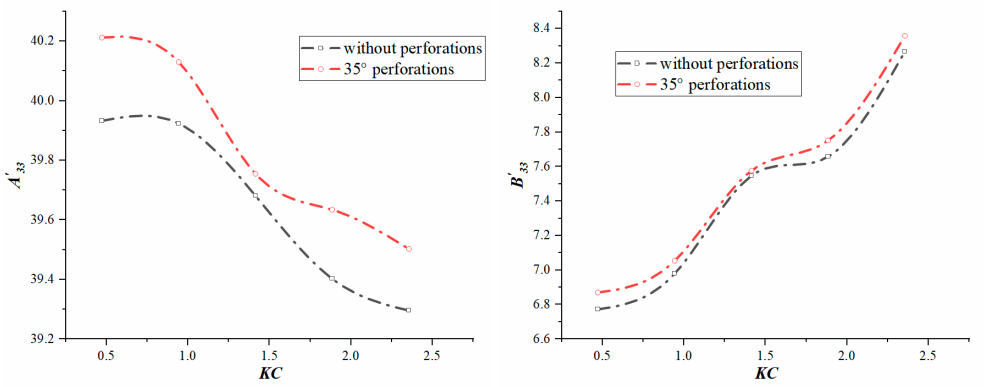

(**c**)

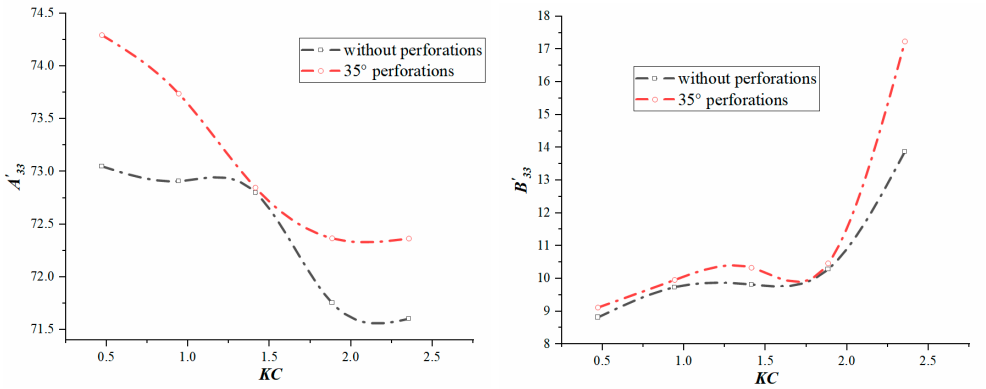

(**d**)

Figure 15. *Cont*.

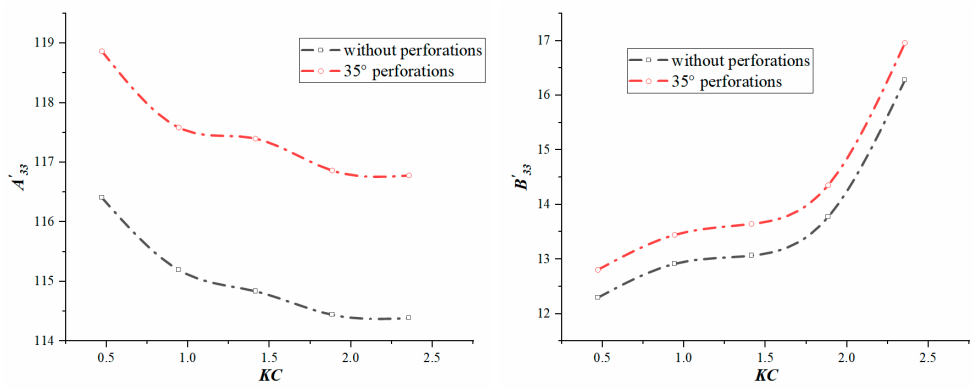

(**e**)

Figure 15. The results of additional mass coefficient and damping coefficient under different chamfers: (**a**) T = 2.5 s; (**b**) T = 5.0 s; (**c**) T = 7.5 s; (**d**) T = 10 s; (**e**) T = 12.5 s.

From Figure 15, the damping coefficient of the three-column float increases with the increase in the number of *Kc*, and the additional mass coefficient decreases with the increase of the number of *Kc* for the same period. The additional mass coefficient and damping coefficient of the three-column float with 35° chamfered perforations are larger than those without perforations. Relative to the oscillation reduction device without perforations, for the device with 35° chamfered perforations at a motion amplitude of 0.03 m and a motion period of 10 s, the maximum increase in the additional mass coefficient is 3.4%, and the maximum increase in the damping coefficient is 1.7%. The results of numerical simulation show that the plate with 35° chamfered perforations has a better effect on the three-floating semi-submersible platform to reduce droop and increase stability compared with the plate without perforations.

Tables 12–16 show the added mass coefficient A'_{33} and added damping coefficient B'_{33} for the model without perforation and the model with 35° chamfered perforations at different KC numbers. The data indicate that, at the same KC number, both coefficients are higher for the model with 35° chamfered perforations. This suggests that the chamfered perforations result in greater forces, leading to an increased damping requirement for the floating body movement.

Table 12. The increase between No perforations and 35° perforations (T = 2.5 s).

Factor	KC	Experiment	Simulation	Increase
A'_{33}	0.47124	3.23249	3.27132	1.20%
	0.94248	3.13311	3.14475	0.37%
	1.41372	2.78399	2.80061	0.60%
	1.88496	2.61405	2.62453	0.40%
	2.35619	2.49059	2.49968	0.36%
B'_{33}	0.47124	0.98327	1.02344	4.09%
	0.94248	1.05685	1.07131	1.37%
	1.41372	1.07665	1.11231	3.31%
	1.88496	1.44691	1.49261	3.16%
	2.35619	1.47209	1.53627	4.36%

Table 13. The increase between No perforations and 35° perforations (T = 5.0 s).

Factor	KC	Experiment	Simulation	Increase
A'_{33}	0.47124	16.53564	16.71033	1.06%
	0.94248	16.22863	16.36726	0.85%
	1.41372	15.84288	16.29854	2.88%
	1.88496	15.82698	16.03386	1.31%
	2.35619	15.54949	15.63084	0.52%
B'_{33}	0.47124	4.25438	4.35471	2.36%
	0.94248	4.50855	4.59658	1.95%
	1.41372	4.60282	4.65473	1.13%
	1.88496	4.742	4.88846	3.09%
	2.35619	5.48108	5.55052	1.27%

Table 14. The increase between No perforations and 35° perforations (T = 7.5 s).

Factor	KC	Experiment	Simulation	Increase
A'_{33}	0.47124	39.93263	40.21229	0.70%
	0.94248	39.92391	40.13032	0.52%
	1.41372	39.68142	39.7554	0.19%
	1.88496	39.40294	39.63438	0.59%
	2.35619	39.2962	39.50291	0.53%
B'_{33}	0.47124	6.77305	6.87072	1.44%
	0.94248	6.98025	7.05458	1.06%
	1.41372	7.54783	7.577	0.39%
	1.88496	7.65802	7.75198	1.23%
	2.35619	8.26827	8.3594	1.10%

Table 15. The increase between No perforations and 35° perforations (T = 10 s).

Factor	KC	Experiment	Simulation	Increase
A'_{33}	0.47124	73.0503	74.29417	1.70%
	0.94248	72.90933	73.73958	1.14%
	1.41372	72.80069	72.84764	0.06%
	1.88496	71.75365	72.3672	0.86%
	2.35619	71.60418	72.36508	1.06%
B'_{33}	0.47124	8.81814	9.11836	3.40%
	0.94248	9.73799	9.96014	2.28%
	1.41372	9.82286	10.33569	5.22%
	1.88496	10.28827	10.4674	1.74%
	2.35619	13.88011	17.23723	24.19%

Table 16. The increase between No perforations and 35° perforations (T = 12.5 s).

Factor	KC	Experiment	Simulation	Increase
A'_{33}	0.47124	116.4088	118.8644	2.11%
	0.94248	115.1969	117.5864	2.07%
	1.41372	114.838	117.3995	2.23%
	1.88496	114.4431	116.8637	2.12%
	2.35619	114.387	116.7807	2.09%
B'_{33}	0.47124	12.29792	12.80672	4.14%
	0.94248	12.9157	13.4465	4.11%
	1.41372	13.06719	13.64646	4.43%
	1.88496	13.77522	14.35624	4.22%
	2.35619	16.28105	16.9608	4.18%

The added mass coefficient represents the additional mass caused by the fluid's inertia during the object's vibration. When the motion period is longer, the fluid's inertia effect decreases, leading to a reduction in the added mass coefficient. This happens because, at longer periods, the vibration frequency of the floating body approaches the natural response frequency of the fluid, reducing the relative motion between them.

The added damping coefficient reflects the resistance caused by the fluid during the vibration of the floating body. The perforated and chamfered design alters the flow characteristics of the fluid, especially by increasing vortex generation and shedding during vibration, which consumes more of the fluid's kinetic energy, increasing the damping effect. As the amplitude and period of vibration increase, particularly at high amplitudes and long periods, vortex and flow separation become more pronounced, resulting in a higher added damping coefficient.

5.3. Reliability Analysis of Numerical Simulation

The numerical simulation and experimental results of the model with 35° chamfered perforations were compared with the motions in the same period and the same amplitude, and the additional mass coefficients A'_{33} and the damping coefficients B'_{33} for different working conditions are shown in Figure 16.

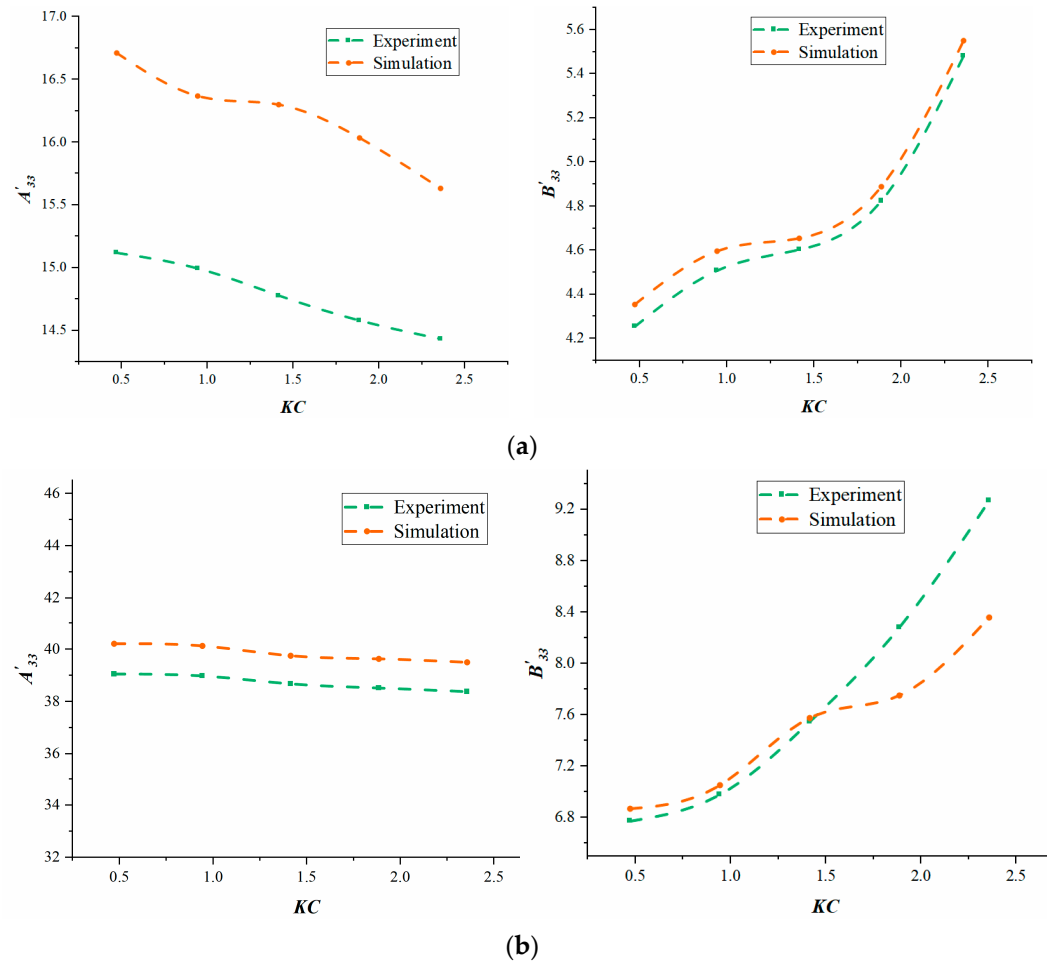

Figure 16. *Cont.*

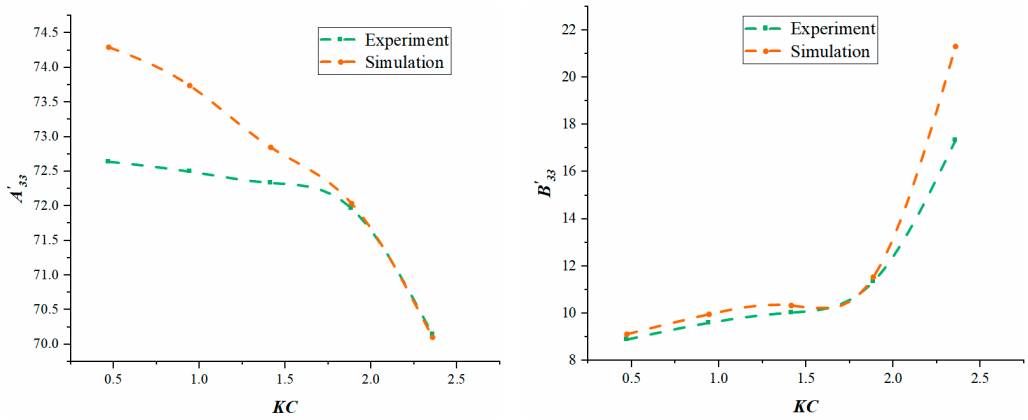

(**c**)

Figure 16. The results of additional mass coefficient and damping coefficient of three-column floating bodies: (**a**) T = 7.5 s; (**b**) T = 10 s; (**c**) T = 12.5 s.

From Figure 16, it can be found that the numerical simulation and test comparison of the three-column floating body with 35° chamfered perforations have basically the same trend of additional mass coefficient and damping coefficient in the same cycle. The data deviation is less than 20%, and the numerical results have a certain reliability. Tables 17–19 show the specific values of the experimental and simulation errors.

Table 17. The tolerance between Experimental and Simulation (T = 5.0 s).

Factor	KC	Experiment	Simulation	Tolerance
A'_{33}	0.47124	15.11786	16.71033	9.530%
	0.94248	14.99349	16.36726	8.393%
	1.41372	14.77754	16.29854	9.332%
	1.88496	14.57819	16.03386	9.079%
	2.35619	14.43166	15.63084	7.672%
B'_{33}	0.47124	4.25438	4.35471	2.304%
	0.94248	4.50855	4.59658	1.915%
	1.41372	4.60282	4.65473	1.115%
	1.88496	4.8239	4.88846	1.321%
	2.35619	5.48108	5.55052	1.251%

Table 18. The tolerance between Experimental and Simulation (T = 7.5 s).

Factor	KC	Experiment	Simulation	Tolerance
A'_{33}	0.47124	39.05444	40.21229	2.879%
	0.94248	38.98321	40.13032	2.858%
	1.41372	38.68167	39.7554	2.701%
	1.88496	38.52101	39.63438	2.809%
	2.35619	38.37995	39.50291	2.843%
B'_{33}	0.47124	6.77305	6.87072	1.422%
	0.94248	6.98025	7.05458	1.054%
	1.41372	7.54783	7.577	0.385%
	1.88496	8.28057	7.75198	−6.819%
	2.35619	9.2677	8.3594	−10.866%

Table 19. The tolerance between Experimental and Simulation (T = 10 s).

Factor	KC	Experiment	Simulation	Tolerance
A'_{33}	0.47124	72.63922	74.29417	2.228%
	0.94248	72.49685	73.73958	1.685%
	1.41372	72.33197	72.84764	0.708%
	1.88496	71.9628	72.03598	0.102%
	2.35619	70.14063	70.10128	−0.056%
B'_{33}	0.47124	8.88872	9.11836	2.518%
	0.94248	9.59843	9.96014	3.632%
	1.41372	10.03336	10.33569	2.925%
	1.88496	11.34401	11.54152	1.711%
	2.35619	17.34219	21.31461	18.637%

From Tables 17–19, it can be found that the data deviation is less than 20%, and the numerical results have a certain reliability.

5.4. Measurement Uncertainty Analysis

The uncertainties in hydrodynamic coefficients were quantified by error propagation. Key contributions include:

(1) Force sensor: ±0.58 N (0.58% at 100 N).
(2) Displacement sensor: ±0.12 mm (0.2% at 60 mm).
(3) Repeatability tests showed a standard deviation of 0.14% in force amplitude.

The expanded uncertainties (k = 2) for A'_{33} and B'_{33} were **1.5%** and **1.3%**, respectively, confirming the reliability of experimental results.

The discrepancy between the experimental uncertainties and the errors obtained in this study suggests the following:

(1) Vortex dynamics: High-KC flow separation may induce nonlinear damping not captured by linear theory.
(2) Sensor dynamics: The 500 Hz sampling rate could alias high-frequency vortex-induced vibrations.
(3) Model fidelity: RANS turbulence modeling may underpredict energy dissipation at perforation edges.

6. Conclusions

6.1. Key Findings

The key findings are as follows:

1. Under the same period, the amplitude of the vertical force on the three-column floating body increases with increasing motion amplitude. Additionally, for the same motion amplitude, the vertical force amplitude increases linearly with the motion period;
2. For the same motion period and amplitude, the vertical force amplitude on the three-column floating body with 35° chamfered perforations is greater than that of the model without perforations;
3. For a given period, the damping coefficient of the three-column float increases with increasing motion amplitude, while the additional mass coefficient decreases. Both the additional mass and damping coefficients of the platform with 35° chamfered perforations are higher than those of the non-perforated version;
4. Compared to the solid heave plate, the 35° chamfered perforations significantly enhance hydrodynamic performance under typical operational conditions (KC = 1.41, T = 10 s):

- Heave motion amplitude: Reduced by 5.2%.
- Added mass coefficient (A'_{33}): Increased by 3.4%.
- Damping coefficient (B'_{33}): Increased by 1.7%.

These improvements confirm the effectiveness of chamfered perforations in stabilizing semi-submersible platforms.

5. Under the same conditions, the error between the coefficients obtained from physical experiments and numerical simulations is within 20%, confirming the reliability of the numerical simulation results.

The reasons for the above results may include: viscous resistance generated when the fluid passes through the perforations, leading to energy dissipation; vortex formation at the edges of the holes during fluid passage, with the process of vortex generation and shedding consuming the fluid's kinetic energy and increasing damping; and the damping effect of open-ended oscillatory reduction plates, which is typically nonlinear, meaning the damping force is directly proportional to the square of the pendulum oscillation velocity. This nonlinear characteristic becomes particularly significant at high-amplitude pendulum motion.

For the operating conditions designed in this paper, the average increase in the added mass coefficient and the added damping coefficient was 1.10% and 3.57%, respectively. When the period is 12.5 s, the increase in both coefficients reached 2.12% and 4.21%. The vertical motion damping effect of the floating body can reach 5%, which is significant for increasing the stability of the semi-submersible platform, increasing the power generation efficiency, and reducing the operation and maintenance cost.

6.2. Limitations and Future Work

Upon completing this study, several limitations were identified:

1. Scale Effects: Model tests followed Froude scaling, but Reynolds number disparities may affect vortex shedding in prototype conditions.
2. Motion Constraints: Forced oscillation tests cannot fully replicate free-decay responses in real sea states.
3. Turbulence Modeling: RANS simulations may underestimate flow separation at high KC numbers; LES or DNS could improve accuracy.
4. Sensor Limitations: The 500 Hz sampling rate may alias high-frequency fluid-structure interactions (>250 Hz).

After considering the experimental results and the study of uncertainties, future studies should incorporate:

1. Free-decay experiments to validate damping coefficients.
2. High-fidelity CFD (e.g., LES) for vortex dynamics analysis.

Author Contributions: W.W.: Conceptualization, Methods, Resources, Investigation, Preparation, Writing-review and editing; J.H.: Writing, Experiments, Writing-original Draft; C.Z.: Validation, Software, Supervision, Experiments; Y.X.: Conceptualization, Supervision; X.G.: Conceptualization, Supervision; D.J.: Experiments, Software. All authors have read and agreed to the published version of the manuscript.

Funding: This study was funded by the National Natural Science Foundation of China (Grant No.52271293) and the major research and development project of Daishan County Zhejiang Province (grant no. 202202).

Data Availability Statement: The data presented in this study are available on request from the corresponding author.

Conflicts of Interest: The authors declare no conflict of interest.

References

1. Wang, X.; Zeng, X.; Li, J.; Yang, X.; Wang, H. A review on recent advancements of substructures for offshore wind turbines. *Energy Convers. Manag.* **2018**, *158*, 103–119. [CrossRef]
2. Ren, Z.; Jiang, Z.; Skjetne, R.; Gao, Z. Development and application of a simulator for offshore wind turbine blades installation. *Ocean Eng.* **2018**, *166*, 380–395. [CrossRef]
3. Arcigni, F.; Abhinav, K.; Collu, M.; Venturini, M. Analysis of tripod supported offshore wind turbines under conditions of marine growth. *Ocean Eng.* **2021**, *220*, 108441. [CrossRef]
4. Olondriz, J.; Elorza, I.; Jugo, J.; Alonso-Quesada, S.; Pujana-Arrese, A. An advanced control technique for floating offshore wind turbines based on more compact barge platforms. *Energies* **2018**, *11*, 1187. [CrossRef]
5. Yang, R.Y.; Wang, C.W.; Huang, C.C.; Chung, C.H.; Chen, C.P.; Huang, C.J. The 1:20 scaled hydraulic model test and field experiment of barge-type floating offshore wind turbine system. *Ocean Eng.* **2022**, *247*, 110486. [CrossRef]
6. Wu, H.; Zhao, Y.; He, Y.; Shao, Y.; Mao, W.; Han, Z.; Huang, C.; Gu, X.; Jiang, Z. Transient response of a TLP-type floating offshore wind turbine under tendon failure conditions. *Ocean Eng.* **2021**, *220*, 108486. [CrossRef]
7. Hegseth, J.M.; Bachynski, E.E.; Martins, J. Integrated design optimization of spar floating wind turbines. *Mar. Struct.* **2020**, *72*, 102771. [CrossRef]
8. Jonkman, J.; Matha, D.A. Quantitative comparison of the responses of three floating platforms. In Proceedings of the European Offshore Wind 2009 Conference and Exhibition, Stockholm, Sweden, 14–16 September 2009; National Renewable Energy Lab: Stockholm, Sweden, 2009. Available online: https://www.osti.gov/servlets/purl/974453 (accessed on 15 July 2023).
9. Si, Y.; Chen, Z.; Zeng, W.; Sun, J.; Zhang, D.; Ma, X.; Qian, P. The influence of power-take-off control on the dynamic response and power output of combined semi-submersible floating wind turbine and point-absorber wave energy converters. *Ocean Eng.* **2021**, *227*, 108835. [CrossRef]
10. Zhang, L.; Shi, W.; Karimirad, M.; Michailides, C.; Jiang, Z. Second-order hydrodynamic effects on the response of three semisubmersible floating offshore wind turbines. *Ocean Eng.* **2020**, *207*, 107371. [CrossRef]
11. Li, J.; Liu, S.; Zhao, M.; Teng, B. Experimental investigation of the hydrodynamic characteristics of heave plates using forced oscillation. *Ocean Eng.* **2013**, *66*, 82–91. [CrossRef]
12. Gao, P.; Liu, C.G. The key issues in the design of the heave plate of spar platforms. *China Offshore Platf.* **2007**, *22*, 9–13.
13. Wei, Y.F.; Yang, J.M.; Chen, G. A review of the hydrodynamic performance of heave damping plates on spar platform. *China Offshore Platf.* **2010**, *25*, 1–4. [CrossRef]
14. Wu, J.H.; Wan, Z.P.; Fang, Y. Wave reflection by a vertical wall with a horizontal submerged porous plate. *Ocean Eng.* **1998**, *25*, 767–779. [CrossRef]
15. Ezoji, M.; Shabakhty, N.; Tao, L.B. Hydrodynamic damping of solid and perforated heave plates oscillating at low KC number based on experimental data: A review. *Ocean Eng.* **2022**, *253*, 111247. [CrossRef]
16. Zhang, S.; Ishihara, T. Numerical study of hydrodynamic coefficients of multiple heave plates by large eddy simulations with volume of fluid method. *Ocean Eng.* **2018**, *163*, 583–598. [CrossRef]
17. Zhu, L.; Lim, H.C. Hydrodynamic characteristics of a separated heave plate mounted at a vertical circular cylinder. *Ocean Eng.* **2017**, *131*, 213–223. [CrossRef]
18. Han, Z.; Zhao, Y.; Su, J.; He, Y.; Xu, Y.; Wu, F.; Jiang, Z. On the hydrodynamic responses of a multi-column TLP floating offshore wind turbine model. *Ocean Eng.* **2022**, *253*, 111262. [CrossRef]
19. Zhang, F. Conceptual Design and Hydrodynamic Performance of Deep-Sea Columnar Platforms. Ph.D. Thesis, Shanghai Jiaotong University, Shanghai, China, 2008. (In Chinese).
20. Liu, S.X.; Zhao, M.; Li, J.X.; Teng, B. Experimental Study on the Hydrodynamic Characteristics of Perforated Heave Plates. *J. Hydrodyn. Res. Prog.* **2012**, *27*, 248–255.
21. Wang, W.; Zhao, C.; Jia, P.; Lu, Z.; Xie, Y. Numerical simulation and experimental study on perforated heave plate of a DeepCwind floating wind turbine platform. *Ships Offshore Struct.* **2023**, *18*, 438–449. [CrossRef]
22. Pan, Z.Y.; Cui, W.C.; Miao, Q.M. Numerical simulation of vortex-induced vibration of a circular cylinder at low mass-damping using RANS cod. *J. Fluids Struct.* **2007**, *23*, 23–37. [CrossRef]
23. Medina-Manuel, A.; Botia-Vera, E.; Saettone, S.; Calderon-Sanchez, J.; Bulian, G.; Souto-Iglesias, A. Hydrodynamic coefficients from forced and decay heave motion tests of a scaled model of a column of a floating wind turbine equipped with a heave plate. *Ocean Eng.* **2022**, *252*, 110985. [CrossRef]

Disclaimer/Publisher's Note: The statements, opinions and data contained in all publications are solely those of the individual author(s) and contributor(s) and not of MDPI and/or the editor(s). MDPI and/or the editor(s) disclaim responsibility for any injury to people or property resulting from any ideas, methods, instructions or products referred to in the content.